Majorana states in prismatic core-shell nanowires

Andrei Manolescu, Anna Sitek, Javier Osca, Llorenç Serra, Vidar Gudmundsson, and Tudor Dan Stanescu

Phys. Rev. B **96**, 125435 — Published 26 September 2017

DOI: 10.1103/PhysRevB.96.125435

Majorana states in prismatic core-shell nanowires

Andrei Manolescu,[1] Anna Sitek,[1,2] Javier Osca,[3] Llorenç Serra,[3,4] Vidar Gudmundsson,[5] and Tudor Dan Stanescu[6]

[1] *School of Science and Engineering, Reykjavik University, Menntavegur 1, IS-101 Reykjavik, Iceland*
[2] *Department of Theoretical Physics, Faculty of Fundamental Problems of Technology, Wroclaw University of Technology, Wroclaw,50-370, Poland*
[3] *Institute of Interdisciplinary Physics and Complex Systems IFISC (CSIC-UIB), Palma de Mallorca, E-07122, Spain*
[4] *Department of Physics, University of the Balearic Islands, Palma de Mallorca, E-07122, Spain*
[5] *Science Institute, University of Iceland, Dunhaga 3, IS-107 Reykjavik, Iceland*
[6] *Department of Physics and Astronomy, West Virginia University, Morgantown, WV 26506, USA*

We consider core-shell nanowires with conductive shell and insulating core, and with polygonal cross section. We investigate the implications of this geometry on Majorana states expected in the presence of proximity-induced superconductivity and an external magnetic field. A typical prismatic nanowire has a hexagonal profile, but square and triangular shapes can also be obtained. The low-energy states are localized at the corners of the cross section, i. e. along the prism edges, and are separated by a gap from higher energy states localized on the sides. The corner localization depends on the details of the shell geometry, i. e. thickness, diameter, and sharpness of the corners. We study systematically the low-energy spectrum of prismatic shells using numerical methods and derive the topological phase diagram as a function of magnetic field and chemical potential for triangular, square, and hexagonal geometries. A strong corner localization enhances the stability of Majorana modes to various perturbations, including the orbital effect of the magnetic field, whereas a weaker localization favorizes orbital effects and reduces the critical magnetic field. The prismatic geometry allows the Majorana zero-energy modes to be accompanied by low-energy states, which we call pseudo Majorana, and which converge to real Majoranas in the limit of small shell thickness. We include the Rashba spin-orbit coupling in a phenomenological manner, assuming a radial electric field across the shell.

I. INTRODUCTION

Zero-energy Majorana bound states, a concept borrowed from particle physics, are at the center of an intense search in condensed matter physics. Similar to the original Majorana fermions, these (quasi)particles are identical to their antiparticles but, unlike their long-predicted fermionic counterparts, they are characterized by non-Abelian exchange properties. Predicted to emerge in certain types of topologically-nontrivial quantum phases,[1–3] the zero-energy Majorana modes benefit from the topological protection of the underlying phase and, consequently, represent an appealing possible platform for fault-tolerant quantum computation.[1,4–6] While topological superconductors appear to be rather rare in nature, several practical schemes for realizing topological superconductivity and Majorana zero modes in solid state heterostructures have been proposed in recent years.[7–9] The basic physics behind these schemes has been discussed in detail in a number of review papers,[10–13] So far, the most promising type of hybrid system involves a semiconductor nanowire with strong spin-orbit coupling proximity-coupled to a standard s-wave superconductor and in the presence of a longitudinal magnetic field.[14,15] When the magnetic field exceeds a certain critical value, the system undergoes a topological quantum phase transition to a topologically-nontrivial superconducting phase. In this phase, the system is predicted to host Majorana modes as pairs of zero-energy mid-gap states localized at the two ends of the nanowire. These Majorana zero modes are topologically-protected, in the sense that they are robust against any local perturbation that does not close the superconducting gap.

Extensive experimental investigations of Majorana modes in semiconductor nanowires have been performed in the past few years. So far, the most promising experimental signature consistent with the presence of Majorana modes in semiconductor-superconductor hybrid structures consists of zero-bias conductance peaks ubiquitously observed in charge transport measurements.[16–26] The conductance peak is produced by electron tunneling into the proximitized semiconductor wire from conducting electrodes attached to its end when a zero-energy Majorana bound state is localized in that region. We note that this type of experiment gives only a primary indication on the possible presence of Majorana bound states and provides no direct evidence of a topological quantum phase transition between the trivial to the topological superconducting phases[11] and no signature associated with the predicted non-Abelian exchange properties of the Majorana zero modes.

In proximitized semiconductor nanowires, which are quasi one-dimensional systems in symmetry class D, the topological superconducting phase that supports the Majorana zero modes has a $\mathbb{Z}_2$ classification. We note that, while ideally the system is one-dimensional, real wires are, of course, three-dimensional and exhibit a variety of non-universal phenomena that can affect the stability of the topological phase and, implicitly, the Majorana zero modes. Multi-band physics[27] is an essential aspect of this phenomenology. Another example is the orbital effect of a magnetic field applied parallel to the nanowire, which has been shown[28] to be detrimental to the stability of the

the Majorana states as it reduces the energy of the low-momentum modes, thus reducing the gap that protects the Majoranas.

The semiconductor nanowires used to realize and detect Majorana bound states are typically grown by bottom-up methods and have a prismatic geometry, most often with a hexagonal cross section, reflecting the underlying crystal structure.[29] With two different concentric materials one can also obtain a prismatic core-shell heterostructure, where the shell is conductive and the core is insulating. Core-shell nanowires have been recently considered for Majoranas based on semiconductor holes, but as a 1D model only.[30] Seen from a different angle, the polygonal shape of the shell may be an advantage for Majorana states. In this geometry the electronic states with the lowest energy are localized in the corners of the shell and those with higher energies are localized on the sides.[31] The corner localization was studied in the 1990s in bent nanowires.[32,33] In our case, the cross section of a core-shell nanowire can be seen as a (sharply) bent and closed channel forming a polygonal ring.

The energy separation between corner and side states is large when the shell thickness is much smaller than the radius of the nanowire, and when the corners are sharp, i. e., it increases when the number of corners decreases. Interestingly, apart from the hexagonal shape, core-shell nanowires with square[34] or triangular[35–39] cross section can also be fabricated. In particular, the gap between corner and side states for a triangular shell of 8-10 nm and radius 50 nm can be in the range 50-100 meV,[40] i. e. larger than many detrimental perturbations for Majorana states, including the orbital magnetic energy. In principle, a prismatic core-shell nanowire could host several Majorana states at each end if the corner states are completely isolated from each other, which happens in the limit of a very narrow shell. Therefore the core-shell nanowires can be an experimental system with multi-chain ladders discussed in recent theoretical papers.[41–43] To the best of our knowledge, the implications of the corner localization in core-shell nanowires on the formation and stability of Majorana bound states have not been explored yet. The main purpose of this work is to fill this gap.

The paper is organized as follows. In Section II we introduce the localization of electrons in polygonal rings and in Section III we describe the nanowires. In Section IV we explain the SOI model. In Section V we present energy spectra of infinite nanowires in the normal state and in Section VI the Bogoliubov-de Gennes spectra in the superconductor state. In Section VII we show and discuss phase diagrams for the three polygonal geometries. The conclusions are collected in Section VIII. Finally, in the Appendix, we present a simplified (toy) model of parallel chains which qualitatively reproduces the basic phase diagrams.

II. POLYGONAL SHELLS

Below we review the properties of the low-energy states in a polygonal ring, which is the cross section of a core-shell nanowire. We performed the numerical diagonalization of the Hamiltonian

$$H_{\rm t} = -\frac{\hbar^2}{2m_{\rm eff}}\left(\partial_x^2+\partial_y^2\right), \tag{1}$$

where $m_{\rm eff}$ is the effective electron mass in the shell material and the partial derivatives in the shell plane (x,y) are calculated numerically within a finite-difference approximation scheme on a grid, with Dirichlet boundary conditions at the edges of the polygons.[40,44] To reach convergence the grid included several thousands of points. In Fig. 1 we show typical probability distributions of corner and side states for a symmetric triangle, square, and hexagon, all with the same side thickness $t = 9$ nm and circumference radius $R = 50$ nm, for InSb parameters (see Sec. III). For each polygon there are $2N$ corner states, where N is the number of corners, followed on the energy scale by $2N$ side states, the counts including the spin.

For this aspect ratio, AR $= t/R = 0.18$, the corner states of the triangle consist in nearly isolated peaks and quasi-degenerate six energy levels, with a small dispersion $\gamma_{\rm T} = 0.02$ meV, separated from the side states by a gap $\Gamma_{\rm T} = 70$ meV, Fig. 2(a). Next, for the square, the corner localization softens a little bit, the eight corner states have a broader dispersion, $\gamma_{\rm S} = 1.4$ meV, and the energy separation from the side states decreases to $\Gamma_{\rm S} = 22$ meV, Fig. 2(b). Further, for the hexagon, the corner peaks drop more and have tails onto the polygon sides, the corresponding twelve corner states have a considerable dispersion, $\gamma_{\rm H} = 8$ meV, comparable to the interval between corner and side states $\Gamma_{\rm H} = 10$ meV, Fig. 2(c). Higher energy states (not shown in the figures) have increasingly spread localization. Apart of the spin degeneracy, the symmetries of the polygons lead to orbital double degeneracies, such that the degeneracy sequences are (24, 42,...), (242, 242,...), and (2442, 2442,...), for triangle, square, and hexagon, respectively.[40] By decreasing the AR of the polygons the corner localization becomes stronger, the probability distribution converges to totally isolated peaks for each polygon, and the energy separation between the highest corner state and the lowest side state considerably increases.[44]

III. MODELS OF CORE-SHELL NANOWIRES

We build the Hamiltonian of the nanowire, $H_{\rm w}$, from several terms,

$$H_{\rm w} = H_{\rm t} + H_\ell + H_{\rm Z} + H_{\rm SOI}. \tag{2}$$

We consider a magnetic field along the nanowire, i. e. along the z axis, $\mathbf{B} = (0,0,B)$, and incorporate it in the

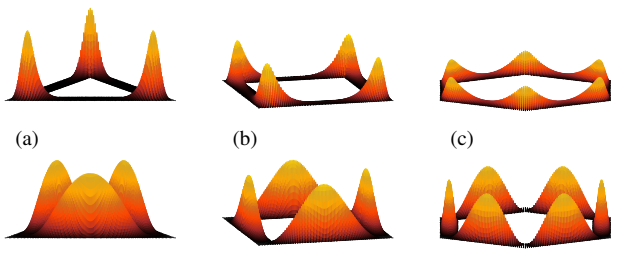

FIG. 1. Probability distributions of corner and side states of an electron in a polygonal ring. The upper row illustrates the corner states (including the ground state) and the lower row the side states: (a) triangle, (b) square, (c) hexagon. All polygons have radius $R = 50$ nm (center-to-corners) and side thickness $t = 9$ nm.

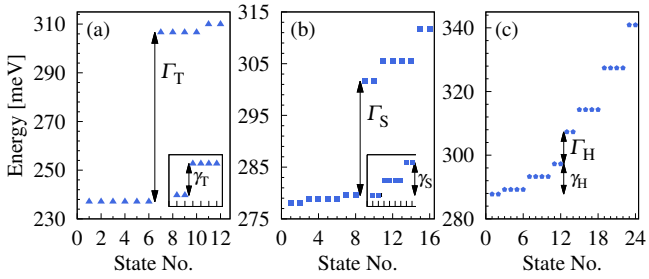

FIG. 2. Low-energy spectra for the polygonal rings shown in Fig.1. The corner states are nearly degenerated for the triangle (a), and have an increasing dispersion for the square (b) and hexagon (c). The insets show the energy span of the corner states which is denoted by $\gamma_{\mathrm{T,S,H}}$. The gap between corner and side states, indicated as $\Gamma_{\mathrm{T,S,H}}$, decreases in the same order. In the numerical calculations we used $m_{\mathrm{eff}} = 0.014$, as for InSb

transverse Hamiltonian H_{t} via the canonical momentum $p_\varphi + eA_\varphi$, where $A_\varphi = Br/2\hat{\boldsymbol{\varphi}}$ is the vector potential in polar coordinates (φ, r) transversal to the nanowire, and $p_\varphi = (-i\hbar/r)\partial_\varphi$.

The second term of Eq. (2) corresponds to the longitudinal degree of freedom, $H_\ell = p_z^2/(2m_{\mathrm{eff}})$. For an infinite nanowire its eigenstates are the plane waves $|k\rangle = \exp(ikz)/\sqrt{L}$, where k is the wave vector, $L \to \infty$ being the nanowire length. For a finite length L we assume hard wall boundaries at $z = \pm L/2$ and the eigenstates become $|n\rangle = \sqrt{2/L}\sin[n(z/L + 1/2)\pi]$, with $n = 1, 2, 3, \ldots$.

Next, the term $H_{\mathrm{Z}} = -g_{\mathrm{eff}}\mu_{\mathrm{B}}\sigma B$ is the spin Zeeman term, with g_{eff} the effective g-factor in the shell material, μ_{B} Bohr's magneton and $\sigma = \pm 1$ the spin quantum number, and finally H_{SOI} is the spin-orbit term, which will be discussed in the next section.

In the calculations we use material parameter values corresponding to (bulk) InSb, which is one of the most interesting semiconductors for Majorana detection due to the large g-factor and strong SOI. We used $m_{\mathrm{eff}} = 0.014$ and $g_{\mathrm{eff}} = -51.6$, i. e. the values known for the bulk material, although they may be different for our thin shell structures. To find them properly one needs to perform ab initio calculations starting with the proper atomic structure in the prismatic geometry. This is a complex problem which is beyond the scope of our present work. We thus compute the electronic states at a mesoscopic scale, i. e. by averaging over many unit cells of the atomic lattice, such that the dominant effects are due to the geometry. This approach has been able to describe the relevant physics related to edge or side localization.[31,35] Still, the precise quantitative validity for core-shell nanowires of simplifying approximations such as the use of piecewise constant potentials and material parameters is something to be confronted with more refined models in the future. The intention of our present work is to predict several scenarios of Majorana physics in shells of prismatic geometry, using the bulk parameters as test values, i. e. mid- way between a qualitative and a quantitative style, and to support each scenario with plausible examples. The qualitative agreement with a toy model (discussed in Appendix) indicates a rather robust physical behavior of the phase diagrams discussed below.

IV. SPIN-ORBIT INTERACTION

In order to obtain Majorana states we need a Rashba-type SOI model for the prismatic geometry. In heterostructures where materials with different work functions are placed next to each other interface electric fields are generated. For a planar 2D electron system created in a semiconductor heterostructure the origin of SOI is the effective (net) electric field, normal to the interface, associated with an asymmetric confinement. For a core-shell heterostructure we assume similar intrinsic fields, present at the core-shell and/or at the shell-vacuum interfaces, perpendicular to the lateral surfaces of the prismatic shell, and thus changing direction at the corners, as illustrated in Fig. 3. In core-shell nanowires there is a geometric asymmetry in the radial direction, inwards vs. outwards, that lends plausibility to an effective radial field. In principle such a field could also be obtained or controlled with gates. In cylindrical coordinates the field has radial and azimuthal components, $\mathbf{E} = (E_\varphi, E_r, 0)$. The SOI Hamiltonian can be calculated as[45,46]

$$H_{\mathrm{SOI}} = \frac{\lambda}{\hbar}\boldsymbol{\sigma}\,(\mathbf{p} \times \mathbf{E})\,, \tag{3}$$

where λ is the SOI coupling constant and $\boldsymbol{\sigma}$ are the Pauli matrices. We implement both E_φ and E_r as functions of φ with two independent strength parameters. This is a phenomenological model aimed at capturing the basic SOI effect dictated by the geometry of the heterostructures, which is necessary for the realization of topological superconductivity and Majorana bound states. In reality the Rashba coupling, and also the g-factor, are expected to depend on the shell thickness and, possibly, on the radius of the wire. To evaluate them rigorously a computationally involved approach is necessary, for example

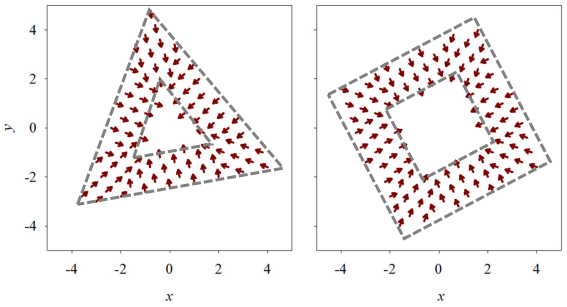

FIG. 3. The effective Rashba electric field for a square and a triangle in the prismatic SOI model. The corner areas span angular intervals of 40^o.

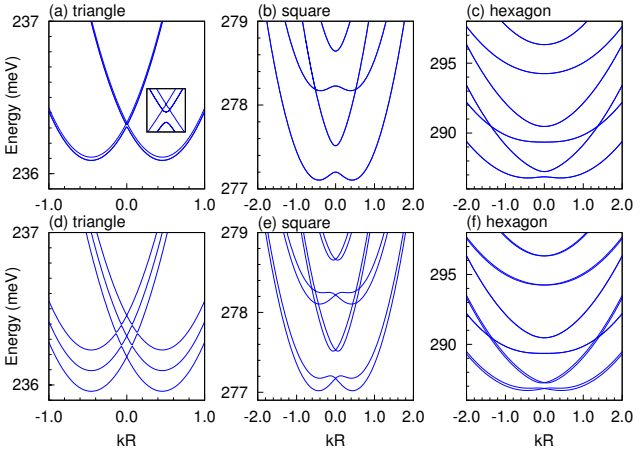

FIG. 4. Energy dispersions for the corner states of infinite nanowires with polygonal shells including SOI within the cylindrical model. The top row shows $2N$ bands for the three polygonal shapes: (a) triangular, $N = 3$, (b) square, $N = 4$, (c) hexagonal, $N = 6$. Due to the geometric symmetries all bands are degenerate, except one pair for the triangle, crossing at $k = 0$, as shown in the zoomed inset. The bottom plots show the results with a transverse electric field of 0.22 mV/R which perturbs the symmetry of each polygon, lifting all spin degeneracies at $k \neq 0$. Here the radius $R = 50$ nm and side thickness $t = 9$ nm. The material parameters are as for InSb.

based on a multiband $k \cdot p$ model[45], taking into account the core-shell materials and geometry. This is an important task, but still, outside our present focus.

In particular, for a cylindrical shell, following the same line of arguments, the effective interface field should be radial and constant, i. e. $\mathbf{E} = (0, E, 0)$. In this case Eq. (3) gives

$$H_{\rm SOI} = \frac{\alpha}{\hbar}(\sigma_\varphi p_z - \sigma_z p_\varphi), \tag{4}$$

where $\alpha = \lambda E$. We shall call (4) and (3) the cylindrical and prismatic SOI models, respectively. The cylindrical model can also be seen as a straight forward transformation of the standard two-dimensional model where the planar Cartesian coordinates are replaced by cylindrical coordinates.[46,47]

For the prismatic nanowires, as long as we consider only corner states in the shell, the SOI is restricted to the corner areas, where we can assume $E_\varphi \approx 0$ and a constant E_r. Therefore, by neglecting the presence of the electrons on the sides of the polygonal shell, where the wave functions exponentially vanish (Fig. 1), the cylindrical model should still be reasonable and qualitatively correct. In the numerical calculations we included the SOI using the cylindrical model, with $\alpha = 50$ meV nm (as for InSb). We also tested the energy spectra with the prismatic SOI model (Fig. 3), and we obtained similar results. In this context it is worth mentioning that the cylindrical SOI model cannot lead to Majorana states for a wire with circular symmetry.[48] As we shall see, this is no longer true for the prismatic geometry.

V. ENERGY SPECTRA OF NANOWIRES IN THE NORMAL STATE

In order to obtain the eigenstates of a nanowire we first diagonalize the Hamiltonian of the polygonal cross section, H_t, on the transverse grid. Then, we combine the N corner states, which are the lowest-energy states of H_t, $|a\rangle$, $a = 1, 2, ..., N$, with the longitudinal modes, which are the eigenstates of H_ℓ, $|k\rangle$ or $|n\rangle$, for the infinite or finite length, respectively. By adding the spin we form a basis set in the total Hilbert space, $|g\rangle = |ak\sigma\rangle$ for the infinite wire and $|g\rangle = |an\sigma\rangle$ for the wire of finite length. We use these bases to calculate the matrix elements of the total Hamiltonian, $\langle g|H_{\rm w}|g'\rangle$. The matrices are diagonalized numerically to give the eigenstates of the two models. For the infinite nanowire $H_{\rm w}$ is already diagonal in k, and we calculate the eigenstates within the subspace $|a\sigma\rangle$ for an array of k values. For the case with finite length we diagonalize a single, but larger matrix including the longitudinal modes $|n\rangle$. The basis set is truncated appropriately for convergence. We used only the corner states as transverse modes $|a\rangle$ because the SOI and other perturbations are too weak to mix them significantly with the side states. By including the side states the largest correction, expected for the highest corner states in the hexagonal shell, is at most 1 meV. For the nanowires with finite length we included all longitudinal modes up to $n = 200$.

In Fig. 4 we display energy eigenvalues of $H_{\rm w}$ for infinite nanowires with the three polygonal cross sections discussed: triangular, square, and hexagonal. In the absence of SOI all energies (or bands) are parabolic functions of k. With SOI they remain even functions, but non-monotonic for $k > 0$ or $k < 0$. For symmetric polygons, i. e. with equal corner angles, the energy bands are shown in Fig. 4(a-c). In these cases the eigenstates of $H_{\rm w}$ appear pairwise degenerate for each fixed k, although the spin is not conserved. For the square and the hexagon four and six bands, respectively, can be observed in the figures, which in reality are eight and twelve, i. e. the number of corners times spin. In the triangular case, due

to the absence of inversion symmetry, one degeneracy is lifted for any $k \neq 0$, and only two degenerate bands are obtained, and thus four energy curves are seen in Fig. 4(a). At $k = 0$ the nondegenerate bands have the familiar crossing (where SOI vanishes), and this is the only exact level crossing point in Fig. 4.

For the purpose of our work the strictly symmetric polygons should be regarded only as mathematical models. The prismatic nanowires grown in labs are naturally not perfectly symmetric even if the polygonal cross section is a result of a specific lattice structure. In addition, in order to detect Majorana states, the experimentalists use gates and contacts that are expected to break the polygonal symmetry. Therefore, in our model we perturb the polygonal symmetries by imposing an electric field along one side of each type of polygon, which generates a voltage of 0.22 mV across the length of one radius. This perturbation lifts the orbital degeneracies of the transversal modes of the nanowires (shown earlier in Fig. 2), and all energy bands for each polygonal shape are now spin split, as seen in Fig. 4(d-f). Still, the splitting decreases for large polygon angles and it is not visible for all hexagon bands in (f).

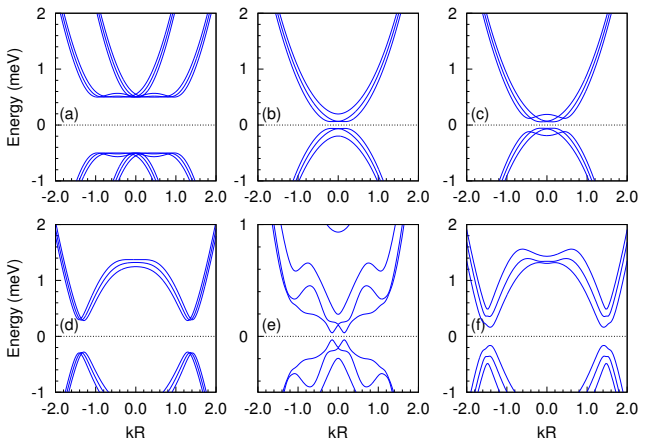

FIG. 5. **Triangular shell.** BdG eigenenergies vs. the wave vector for a triangular shell of infinite length. The superconductor gap closes and reopens depending on the values of the chemical potential μ and magnetic field B. The nanowire radius $R = 50$ nm is fixed. The shell thickness is $t = 9$ nm, i. e. AR $= 0.18$ for the cases (a)-(d). Other parameters: (a) $\mu = 236.2$ meV, $B = 0$, (b) $\mu = 234.6$ meV, $B = 1.32$ T, (c) $\mu = 234.7$ meV, $B = 1.32$ T, (d) $\mu = 236.2$ meV, $B = 1.32$ T. Next, $t = 12.5$ nm, i. e. AR $= 0.25$, for (e) $\mu = 126.7$ meV, $B = 0.34$ T, and (f) $\mu = 126.7$ meV, $B = 1.32$ T.

VI. MAJORANA STATES

The Majorana states are obtained using the Bogoliubov – de Gennes Hamiltonian (BdG), $H_{\rm BdG}$, which we obtain with the matrix elements of $H_{\rm w}$ and with the isospin quantum number $\tau = \pm 1$. For the infinite wire they can be written as

$$\begin{aligned}\langle a\sigma\tau|H_{\rm BdG}(k)|a'\sigma'\tau\rangle &= \tau\,{\rm Re}\langle a\sigma\tau|H_{\rm w}(\tau k)|a'\sigma'\tau\rangle \\ &+ i\,{\rm Im}\langle a\sigma\tau|H_{\rm w}(\tau k)|a'\sigma'\tau\rangle - \tau\mu\delta_{aa'}\delta_{\sigma\sigma'},\end{aligned} \tag{5}$$

$$\langle a\sigma\tau|H_{\rm BdG}(k)|a'\sigma'\tau'\rangle = \tau\sigma\delta_{\sigma,-\sigma'}\delta_{aa'}\Delta,\ \tau \neq \tau'. \tag{6}$$

Eqs. (5-6) define the diagonal and off-diagonal elements in the isospin space, respectively. μ is the chemical potential, 2Δ is the superconductivity gap, and δ denotes the Kronecker symbol. Here the wave vector k is included in the Hamiltonian because it behaves like a parameter. For the nanowire of finite length these equations are replaced by

$$\begin{aligned}\langle g\tau|H_{\rm BdG}|g'\tau\rangle &= \tau\,{\rm Re}\langle g\tau|H_{\rm w}|g'\tau\rangle \\ &+ i\,{\rm Im}\langle g|H_{\rm w}|g'\tau\rangle - \tau\mu\delta_{gg'},\end{aligned} \tag{7}$$

$$\langle g\tau|H_{\rm BdG}|g'\tau'\rangle = \tau\sigma\delta_{\sigma,-\sigma'}\delta_{aa'}\delta_{nn'}\Delta,\ \tau \neq \tau'. \tag{8}$$

where we used the previous notation $|g\rangle = |an\sigma\rangle$ for the basis states of the nanowire in the normal state.

A. BdG spectra for nanowires of infinite length

In Fig. 5 we show several examples of BdG spectra for a triangular nanowire of infinite length. We use the bare superconductor energy parameter $\Delta = 0.5$ meV. Only the transversal corner states are considered in the calculations, the mixing with the side states being completely negligible for the chemical potentials and magnetic fields used. The spectra are selected for the further discussion on the phase diagrams with several representative values of the chemical potential and magnetic field B. The triangular symmetry is broken by the small electric bias discussed in the previous section. In the first example, Fig. 5(a), the BdG states are obtained with μ near the intersection of the six energy curves seen in Fig. 4(d) and $B = 0$. This case corresponds to the trivial phase of the proximity-induced superconductivity in the nanowire. The spectra are particle-hole symmetric, but for clarity we display a larger interval for particle than for hole states.

By varying the chemical potential and/or increasing the magnetic field, and thus the Zeeman energy, the gap closes first at $k = 0$, and then it opens again, and the systems enters into the topological phase. In Figs. 5(b,c) we show two situations with $B = 1.32$ T, and a very small difference between the chemical potentials, $\mu = 234.6$ and 234.7 meV, respectively, such that one can see a small gap at $k = 0$ reopening due to the repulsion of different corner states. In Fig. 5(d), with the same magnetic field, and $\mu = 236.2$ meV, the gap at $k = 0$ is largely open. In these cases Majorana states are expected, located at the ends of the nanowire, and with zero energy, which we shall observe with the nanowire model of finite length. Notice the smaller gaps at finite k in Figs. 5(d,e,f). They indicate orbital effects of the magnetic field which may possibly forbid the formation

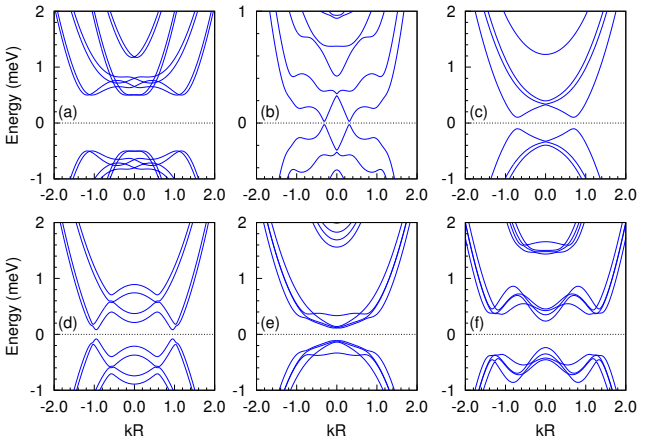

FIG. 6. **Square shell.** BdG energy spectra similar to those shown in Fig. 5, for a nanowire of radius $R = 50$ nm. The shell thickness is $t = 9$ nm, i. e. AR $= 0.18$ for the cases (a) $\mu = 277.6$ meV, $B = 0$, (b) $\mu = 277.6$ meV, $B = 0.33$ T, (c) $\mu = 276.5$ meV, $B = 0.79$ T, (d) $\mu = 276.5$ meV, $B = 1.32$ T. Next, $t = 8$ nm, i. e. AR $= 0.16$ for (e) $\mu = 346.4$ meV, $B = 0.66$ T, and (f) $\mu = 347.3$ meV, $B = 0.66$ T.

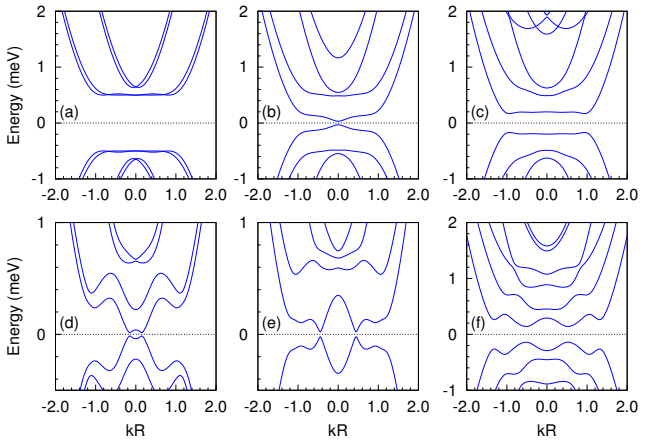

FIG. 7. **Hexagonal shell.** BdG spectra, as in Figs. 5-6, for a nanowire of radius $R = 50$ nm and shell thickness $t = 9$ nm, i. e. AR $= 0.18$. (a) $\mu = 286.9$ meV, $B = 0$, (b) $\mu = 286.9$ meV, $B = 0.062$ T, (c) $\mu = 286.9$ meV, $B = 0.26$ T, (d) $\mu = 287.3$ meV, $B = 0.039$ T, (e) $\mu = 287.3$ meV, $B = 0.17$ T, (f) $\mu = 287.3$ meV, $B = 0.33$ T.

of Majorana states if such gaps become very small (much smaller than 2Δ).[28] By increasing the thickness of the shell, from 9 to 12.5 nm, the energy separation between the corner states, and hence between the bands shown grows, as seen in Figs. 5(e,f). At the same time the corner localization weakens and the orbital effects increase, so the Majorana suppression at large magnetic fields becomes more likely, Figs. 5(e).

In Fig. 6, we show several cases with the square geometry, with four corner states (not counting the spin), which lead to more complicated spectra. The topologically trivial phase is shown in Fig. 6(a), for a shell thickness of 9 nm. Fig. 6(b), with nearly closed gaps at finite k, and Fig. 6(c), with a larger gap at a larger k, correspond to a topological phase. The square geometry implies a larger energy separation between the corner states compared to the triangular geometry with the same AR, and thus the orbital effect may be more detrimental for the square than for the triangular shell. By slightly reducing the shell thickness from 9 to 8 nm we can obtain more robust topological phases for the square geometry, Fig. 6(d,e,f).

In Fig. 7, we show several spectra corresponding to the hexagonal shell, now with six corner states involved. The magnetic fields necessary to close the superconductor gap has now lower values than for the other geometries, a tendency that can also be observed for the square vs. triangular case. The reason is that the corner localization softens when the angle of the polygons increase, and orbital effects of the magnetic field are more important. In other words, the split of the energy bands occurs not only due to the spin Zeeman energy, but also because of the orbital Zeeman energy. We shall refer to these spectra later when we shall discuss the phase diagrams.

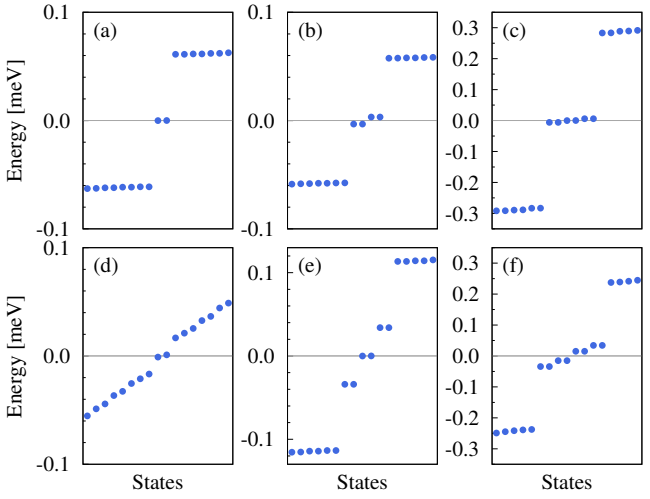

FIG. 8. Examples of BdG energy spectra for a nanowire of 10000 nm length and 50 nm radius for selected values of the chemical potential and Zeeman energy and two shell geometries: *triangular, the top row,* with thickness $t = 9$ nm and (a) $\mu = 234.6$ meV, (b) $\mu = 234.7$ meV, (c) $\mu = 236.2$ meV, all with $B = 1.32$ T; *square, the bottom row,* with (d) $t = 9$ nm, $\mu = 277.6$ meV $B = 0.33$ T, and also $t = 8$ nm where (e) $\mu = 346.4$ meV and (f) $\mu = 347.3$ meV both with $B = 0.66$ T.

B. BdG spectra for nanowires of finite length

Next, we shall correlate the BdG spectra shown for infinite nanowires with some results for nanowires of finite length $L = 200R = 10000$ nm, with triangular and square shells, shown in Fig. 8. In the top row, Fig. 8(a-c), we show three possible situations obtained for the triangular geometry. One pair of states at zero energy is interpreted as a pair of Majorana (M) states, one at each end of the

wire, like in Fig. 8(a). For the infinite wire this situation is shown in Fig. 5(b). In this case the M states are formed due to the particle-hole interaction within a single corner state.

When two corner states are involved at the same time, two particle-hole symmetric pairs of states may be created, one pair with positive and another one with negative energies, and both close to zero, as can be seen in Fig. 8(b). For the infinite nanowire this situation corresponds to Fig. 5(c). We shall call such states pseudo (P) Majorana, and we shall denote the resulting combination of two P pairs as PP. We also notice that the gap between the other particle and hole states is quite small in Figs. 8(a-b), where one or two corner states contribute to the low-energy states, respectively.

Fig. 8(c) shows one M and two P states, and a considerably larger gap. We shall denote this combination as PMP. In this case all three corner states mix together. The corresponding spectra for the infinite wire have been shown in Fig. 5(d). For a very thin shell, i. e. very low AR, the corner states would become isolated from each other and each one would create an independent M state. By slightly increasing the AR the wave functions of different corner states develop a very small exponential overlap along the sides of the polygonal shell, not visible in Fig. 1(a), which is equivalent to an interaction between the corner states. This interaction lifts the degeneracy of the three former M states, transforming two of them in P states, but leaving one M at zero energy, hence giving a PMP configuration. The energy of the P states can still be close to zero if the energy separation between the corner states γ is smaller that the superconductivity parameter Δ such that the pairing interaction mixes all corner states, provided the chemical potential is such that they are all populated. For the triangular shell with $t = 9$ nm thickness we have $\gamma_{\rm T} = 0.027$ meV.

For the square geometry an M state exists in the situation shown in Fig. 6(c) and a PP combination in that of Fig. 6(d). The case of Fig. 6(b) with vanishing gap at $kR \approx 0.3$ is shown in Fig. 8(d). A kind of M precursor state can be observed, eventually becoming a real M state for a nanowire longer that 10000 nm. The PMP configuration of Fig. 8(e) corresponds to Fig. 6(e). Finally, in Fig. 8(f) we obtain four pairs around zero energy, to be called a 2PP combination, indicating four corner states competing to create Majorana states. Again, like for the triangular case, for a very low AR, the square shell yields four independent or degenerate Majoranas at zero energy, whose degeneracy is lifted at finite AR. But unlike the triangular case, now, due to the particle-hole symmetry, no pure Majorana can survive out of the former four, and the result is a 2PP group, with energy dispersion smaller than the superconductor gap.

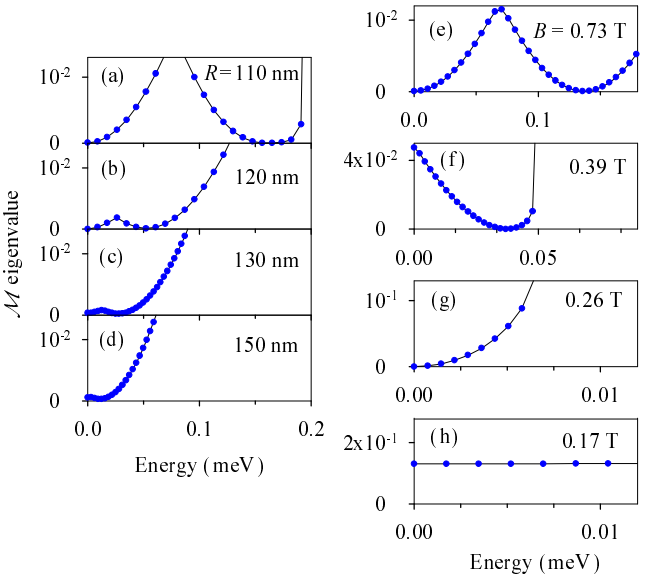

FIG. 9. Energy dependence of the lowest eigenvalue of matrix $\mathcal{M}$ in a semi-infinite triangular wire. The zeroes indicate the physically acceptable energies for states attached to $z = 0$ while decaying for increasing z. Panels (a) to (d) correspond to a PMP configuration with increasing shell radius and fixed $t = 40$ nm and $B = 0.73$ T. Panels (e) to (h) correspond to a fixed $R = 110$ nm and $t = 37.5$ nm, and decreasing magnetic fields, with configurations PMP (e), PP (f), M (g) and trivial (h). Other parameters: $\mu = 22.7\,$meV, $\alpha = 50\,$meVnm, $\Delta = 0.5\,$meV.

C. Semi-infinite nanowires

We have confirmed the above scenario of zero-energy (M) and near-zero-energy (P) pairs of states in the limit of very long wires directly studying the semi-infinite system. In this limit, any longitudinal finite size effect due to interference between opposite wire ends is totally removed and we can unambiguously assign the fragmentation of the P pairs to the interaction between the localized states along the edges of the prism. The semi-infinite system has been described with the complex-k approach introduced in Ref. 49 for the case of 2D planar wires. In this approach the existence of a state attached to the semi-infinite system boundary is signaled by a zero eigenvalue of a matrix $\mathcal{M}_{kk'}$, defined by the set of evanescent modes $\{k\}$ as labeled by their complex wavenumbers.

In Fig. 9 we show the lowest eigenvalue of matrix $\mathcal{M}$ as a function of the energy. Since the results are symmetric by reverting the sign of E we only show the positive energies. Figures 9(a-d) show the evolution with increasing shell radius R of the zeros of matrix $\mathcal{M}$ for a selected case. The chosen parameters correspond to a PMP configuration in a triangular wire, with an $\mathcal{M}$ zero exactly at zero energy and two additional ones at finite energies (a corresponding zero at negative energy is not shown). By increasing R the prism edges become more and more

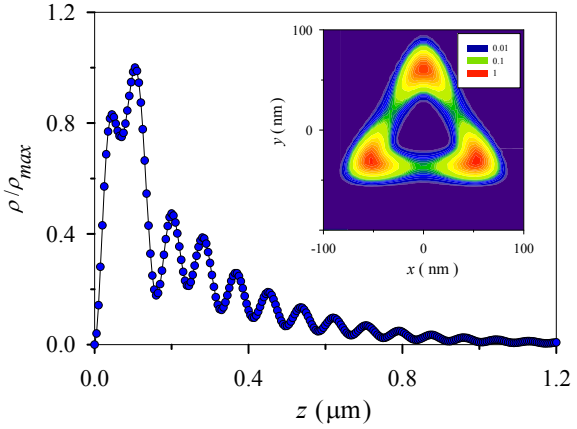

FIG. 10. Density corresponding to the M state of Fig. 9(a) (at zero energy). Dots show the z evolution of the 1D density integrated in the transverse directions, while the inset shows in a color scale the transverse pattern for $z = 150$ nm, near the maximum of the integrated 1D density.

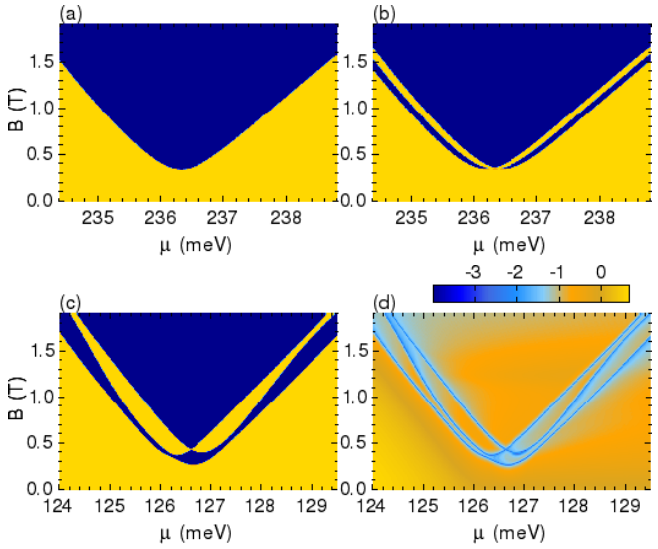

FIG. 11. **Triangular shell** with $R = 50$ nm. In panels (a)-(c) the dark blue color indicates the topological Majorana phases and the yellow color the trivial phases, the frontiers being defined by the gap closed at $k = 0$. In (d) the colors indicate the minimum gap at all k values, on the $\log_{10}$ scale. (a) Symmetric triangle with $t = 9$ nm, with corner states almost three-fold degenerated. (b) The same triangle in the presence of the weak transverse electric field which removes the degeneracy such that the phase boundary splits in three. (c-d) A thicker shell, with $t = 12.5$ nm.

independent, causing a collapse towards zero energy of all three states. Figures 9(e-h) show the variation of the null eigenvalue for decreasing magnetic field with a fixed radius. The chosen shell width is rather large for a better separation of the split P modes. Increasing the field the configurations in Fig. 9 are: trivial (h), M (g), PP (f), PMP (e).

A characteristic density of an M mode is shown in Fig. 10. The transverse-integrated density shows a shape similar to the known behavior from purely 1D models, with a decay length of around 1 μm for the chosen parameters. As anticipated, the transverse pattern exhibits localization on the edges of the triangular wire, with sizable overlaps on the sides representative of edge-edge interactions in small enough wires ($R = 110$ nm).

VII. PHASE DIAGRAMS

In this section we show phase diagrams in the parameter space μ–B obtained by calculating the minimum gap of the BdG energy spectra for the infinite nanowire, at all k values. At any chemical potential μ the phase transition from the trivial (no Majorana) to the topological state (with Majorana) is expected to occur when the magnetic field is strong enough to close the superconductor gap at $k = 0$. In principle the minimum or critical magnetic field necessary for closing the superconductor gap corresponds to a spin Zeeman energy $E_Z = 2\Delta = 1$ meV. For our material parameters this means $B = 0.33$ T. This result is however true as long as the main effect of the magnetic field longitudinal to the nanowire is to create only a spin splitting, and no orbital energy, e. g. for 1D or 2D (flat) nanowires. For a prismatic core-shell nanowire this can happen only if the corner states are almost isolated. In our case this situation occurs for the narrow triangular shell.

In Fig. 11(a) we show the phase diagram for the triangular symmetric nanowire, where the topological phase is shown with the dark blue color and the trivial phase with yellow. By breaking the symmetry of the triangle, with the weak transversal electric field, the phase boundary splits into three frontiers, each one generated by different corner states, Fig. 11(b). The frontiers indicate the gap closed at $k = 0$. In both cases the topological phase above all lines is a PMP type presented in Fig. 8(c), with low-energy P states, implied by the small energy dispersion of the corner states $\gamma_T < \Delta$.

In addition, for the asymmetric triangle, at any fixed chemical potential, a succession of phases occurs when the magnetic field is increased from zero. After crossing the first frontier one enters a topological state of an M type, illustrated in Fig. 8(a). Then, after crossing the second border a PP phase is obtained, [Fig. 8(b)], which is in principle a topologically trivial phase. However these low-energy P states are expected to converge to two Majorana pairs in the limit of a very small ratio t/R, and the phase to become topological.

Increasing now the thickness, to $t = 12.5$ nm, the energy dispersion of the corner states increases to $\gamma_T = 0.56$ meV and the three frontiers become more separated, as seen in Fig. 11(c). The energy interval between the inner and outer frontier is close to γ_T. Moreover, the orbital effects of the magnetic field increase and the critical mag-

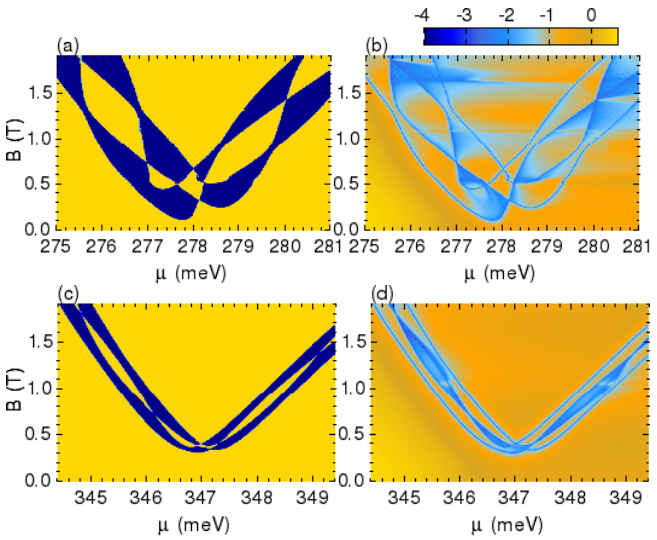

FIG. 12. **Square shell** with $R = 50$ nm. The topological (Majorana) and trivial phases are shown in dark blue and yellow, respectively, with frontiers defined by the gap closed at $k = 0$, whereas the smallest gap at all k values is shown with continuous colors (on $\log_{10}$ scale), like before. (a-b) $t = 9$ nm, (c-d) $t = 8$ nm.

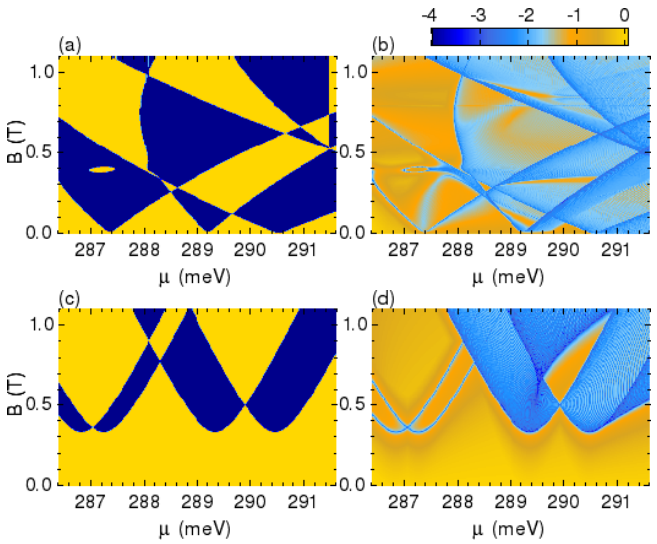

FIG. 13. **Hexagonal shell** with $R = 50$ nm and $t = 9$ nm. (a-b) The phase diagrams are shown with the same color schemes as before (Figs. 11-12). (c-d) The results after excluding the orbital Zeeman effect of the magnetic field.

netic field slightly reduces to $B = 0.27$ T. But, the gaps can possibly shrink at nonzero k values, as shown in the example of Fig. 5(e), corresponding to the bottom of the topological phase, for $\mu = 126.7$ meV and $B = 0.34$ T. Such small energy gaps at $k \neq 0$ indicate the possible instability of the Majorana states. Therefore, to incorporate that information, in Fig. 11(d) we repeat the phase diagram on a color scale indicating the minimum gap at any k. In this case the gaps are still reasonably large in most of the regions such that the main topological phase is still robust. One can see for example the BdG spectrum corresponding to $\mu = 126.7$ meV and $B = 1.32$ T shown in Fig. 5(f). The spectrum for the finite wire is now qualitatively like in Fig. 8(e), with a clear M state, but with the former P states now with larger energy, that will further increase by increasing the thickness of the shell.

For the square shell with thickness $t = 9$ nm the phase diagrams are shown in Fig. 12. We see now four phase boundaries, corresponding to the four corner states, separated by an energy γ_S. At the bottom of the phase diagram we notice a lower critical magnetic field than for the triangular shell, of about 0.1 T, a consequence of the increased orbital Zeeman energy. But at the same time, in the topological phase, the gaps at finite k values can be small. For example for the magnetic field $B = 0.33$ T at $\mu = 277.6$ meV the BdG spectrum for the infinite wire is shown in Fig. 6(b) and indicates a very small gap at $kR \approx 0.3$. Still, in the version with finite length, Fig. 8(d), we see two energies close to zero, which would become an M state for a sufficiently long nanowire. Indeed, that phase region is theoretically a topologically nontrivial one, and in other regions the gap at finite k may increase. For example, slightly to the left, for $\mu = 276.5$ meV and $B = 0.79$ T, the spectrum is shown in Fig. 6(c) and it has a finite length counterpart similar to that shown in Fig. 8(a).

By crossing now each frontier defined by the gap closed at $k = 0$, with magnetic field increasing from zero, topologically nontrivial phases containing M states alternate with topologically trivial phases containing at most P states, depending on whether the number of crossed frontiers is odd or even, respectively. For example, with $\mu = 276.5$ meV and $B = 1.3$ T, the spectrum is that of Fig. 6(d), with a PP configuration in the finite case. Thus, the phase surrounded by all four frontiers, situated in the middle of Fig. 12(a), is a trivial phase, where we expect only P states.

By reducing the aspect ratio of the polygon, for example by reducing the thickness by only one nanometer the energy spread of the corner states rapidly drops to $\gamma_S = 0.56$ meV (at $B = 0$) and the phase boundaries approach each other, Fig. 12(c). The central region contains states of 2PP type, one of which being shown in Fig. 8(f) for $\mu = 347.3$ meV and $B = 0.66$ T. Reducing the aspect ration of the square polygon further these states converge to four independent M states. Notice also that the critical field increases relatively to the previous case of $t = 9$ nm because the orbital Zeeman effect drops.

The orbital effect further increases for the hexagonal shell with a similar aspect ratio as the other polygons, $t = 9$ nm, such that the critical magnetic field is about 12 mT for $\mu = 287.3$ meV, Fig. 13(a). That phase boundary is created by the corner state with the lowest energy. As for the square geometry, the energy gap in the topological phase may possibly be almost closed at nonzero k

as shown in Figs. 7(d) and (e), and also indicated by the blue colors of Fig. 13(b). Still, robust Majorana regions exists in this example at chemical potentials below 288 meV. BdG spectra in one of such zones, at $\mu = 286.8$ meV, are shown in Fig. 7(b) and (c), for $B = 0.062$ T when the gap closes at $k = 0$ (i. e. near the phase boundary), and at $B = 0.26$ T, when M states are present. In the later case the eigenstates of a nanowire of finite length are qualitatively similar to that of Fig. 8(a).

In general both orbital and spin Zeeman energies may lead to the splitting of electron and hole bands of the superconductor, which would combine into M states at a sufficiently large magnetic field. It turns out that for our hexagonal core-shell wire the orbital splitting is dominant. Consequently, in this case, the M states can be obtained even if we neglect the g-factor. With $g_{\rm eff} = 0$ we could obtain a critical field of about 60 mT. This is an important detail, since the g-factor in the shell material may be different, possibly lower than that of the same bulk material. A "strange" detail of the phase diagram can be the small elliptic island seen on the left side of Fig. 13(b), around $\mu \approx 287.2$ meV and $B \approx 0.4$ T. The reason for it is that, due to the combined orbital and spin Zeeman splitting, the energy levels at $k = 0$, forming the M states, can possibly increase with the magnetic field, instead of decreasing, as expected from the spin Zeeman effect alone. Within that island the topological phase is suppressed, although it exists all around outside it.

Finally, to close this section, in Fig. 13(c-d) we show the phase diagram for the hexagon after removing from the Hamiltonian (2) all terms related to the orbital Zeeman effect of the magnetic field, to compare with the real phase diagram. Indeed, the critical field returns to the value expected from the spin Zeeman splitting only. But with increasing the chemical potential the gap can easily close at finite k values in the topological phase even without orbital effects.

VIII. SUMMARY AND CONCLUSIONS

In conclusion, we have shown that prismatic core-shell nanowires with proximity-induced superconductivity and Rashba spin-orbit coupling provide an interesting and rather complex playground for Majorana physics. A key new element that characterizes these structures is that the Majorana physics can be realized within a low-energy sub-space defined by states localized along the edges of the prism, which are separated by a significant energy gap from higher energy states. Furthermore, the localization of these states around the edges can be controlled, e. g., by varying the thickness of the shell or of the core. Strong edge localization leads to a system of effectively decoupled 1D nanowires running along the edges of the prism, each wire hosting Majorana bound states generated according to the well-known mechanism when the magnetic field exceeds a certain critical value. Remarkably, upon increasing the aspect ratio $\mathrm{AR} = t/R$ the "edge" wires become coupled and an interference between states localized on different edges emerges. In the phase diagram, this edge-edge "communication" is manifested as a fragmentation of the boundaries between trivial and topological regions, as well as a separation of the Majorana bound states into real Majoranas and "trivial", but nearly-zero energy modes which we dub *pseudo Majorana* states.

The transformation of Majorana into pseudo Majorana states can be seen as a finite size effect in the direction transversal to the nanowire. The resulting phase diagrams correspond to ladders of interacting chains,[41–43] as we demonstrate in the Appendix.

In the presence of edge-edge interference there are regions in the $\mu - B$ phase diagram containing n_p near-zero-energy pairs of states, where n_p can take all integer values from zero to the number of prism edges. We have focussed on triangles and squares, exploring also the results for hexagons. Regions with odd values of n_p contain a genuine Majorana mode at zero energy, while those with even values of n_p only contain zero modes asymptotically, for low AR. Actually, the energies of all the n_p pairs collapse to zero energy in the limit of low AR. We stress that the Rashba interaction in our model is not oriented along any externally fixed direction, but points perpendicular to the sides and in a radial direction on the edges. Therefore, we do not need to invoke a breaking of the overall nanowire symmetry. For given values of the shell thickness and radius, the edge localization weakens when the number of corners is increased. This is supported by our results for triangle, square and hexagon. Indeed, the triangle has a relatively weaker fragmentation of the phase diagram and of the pseudo Majorana pairs, while this fragmentation is larger for the hexagon.

A relevant effect in core-shell nanowires is the possibility of controlling the magneto-orbital contributions by varying the shell thickness t. Orbital effects of the magnetic field cause a strong reduction of the global energy gap for propagating states at arbitrary values of the wave vector k. They can even lead to a complete closing of the gap at a finite k in some cases. We have shown that in prismatic core-shell wires with small values of t orbital effects are greatly quenched and, as a consequence, the energy gaps are sizeable larger than for wide shell nanowires. This is a very appealing feature, since in any practical application a sizeable gap is required for the stability and protection of the Majorana states.

Our analysis uncovered a remarkable consequence of the magnetic orbital effect in prismatic core-shell nanowires. Namely, the strong reduction of the overall minimum magnetic field for a phase transition, for an arbitrary chemical potential μ. This is a consequence of edge-edge interference in thick enough core-shell nanowires. For the hexagon this reduction is much larger than for the triangular and square, due to the enhanced edge-edge interference. As mentioned, thick wires also tend to rapidly close the overall gap for propagating states when increasing B. Still, our results indicate that in hexagonal prismatic nanowires a compromise regime

can be found with a thickness t such that the Majorana pairs are obtained, along with a sizable overall gap, at low magnetic fields. Finally, as a general conclusion, we emphasize that edge localization in prismatic core-shell nanowires offers a promising physical mechanism towards the controllability of Majorana states in nanowires.

ACKNOWLEDGMENTS

This work was partially financed by the research funds of Reykjavik University. L.S. was supported by grant FIS2014-52564 (Mineco, Spain). TDS was supported in part by NSF DMR-1414683.

Appendix: Toy model for proximitized core-shell nanowires

To gain further insight into the low-energy physics of proximitized core-shell nanowires, and to better understand the qualitative dependence of the BdG spectrum on relevant parameters, it is convenient to use a simplified tight-binding "toy model" consisting of coupled parallel chains. The basic idea is to define a "coarse-grained" shell consisting of one chain associated with each vertex and one chain corresponding to each side, as illustrated in Fig. A1. If the cross section of the wire is a polygon with N corners, the toy model will contain N or $2N$ parallel chains, depending on whether only the corner or also the side states are included, respectively.

Consider now a core-shell nanowire, described in a tight-binding manner in the longitudinal direction, and proximity-coupled to one ore more s-wave superconductors. The low-energy physics of the hybrid structure is described by the following BdG Hamiltonian

$$
\begin{aligned}
H = & -t\sum_{i,\ell,\sigma}\left(c^{\dagger}_{i+1\ell\sigma}c_{i\ell\sigma}+h.c.\right)-t'\sum_{i,\ell,\sigma}\left(c^{\dagger}_{i\ell+1\sigma}c_{i\ell\sigma}+h.c.\right)\\
& +\sum_{i,\ell,\sigma}\left[V_{\rm eff}(\ell)-\mu\right]c^{\dagger}_{i\ell\sigma}c_{i\ell\sigma}+\Gamma\sum_{i,\sigma}\sum_{\ell}^{(even)}c^{\dagger}_{i\ell\sigma}c_{i\ell\sigma} \qquad \text{(A.1)}\\
& +\frac{i}{2}\sum_{i,\ell}\left[\alpha\, c^{\dagger}_{i+1\ell}\left(\hat{\sigma}\cdot n_{\ell}\right)c_{i\ell}+\alpha'\, c^{\dagger}_{i\ell+1}\hat{\sigma}_x c_{i\ell}+h.c.\right]\\
& +E_Z\sum_{i,\ell}c^{\dagger}_{i\ell}\hat{\sigma}_x c_{i\ell}+\sum_{i,\ell}\left(\Delta_{\ell}c^{\dagger}_{i\ell\uparrow}c^{\dagger}_{i\ell\downarrow}+\Delta^{*}_{\ell}c_{i\ell\downarrow}c_{i\ell\uparrow}\right),
\end{aligned}
$$

where $c_{i\ell\sigma}$ is the annihilation operator for an electron with spin projection σ localized on the longitudinal lattice site i of the chain ℓ, $1\le\ell\le 2N$, and $c_{i\ell}=(c_{i\ell\uparrow},c_{i\ell\downarrow})^T$ is the corresponding spinor operator. The first term in Eq. (A.1) represents nearest-neighbor hopping along the chains, while the second term corresponds to the inter-chain coupling. In the summations over the chain index ℓ we use the convention $2N+1\equiv 1$. The inter-chain coupling t' contains information about the shell thickness, so that $t'/t\to 0$ in the thin shell limit. The third term of the Hamiltonian (A.1) contains the chemical potential μ and a chain-dependent effective potential $V_{\rm eff}(\ell)$ that incorporates electrostatic effects due to back gates, coupled superconductors, and non-homogeneous charge distributions. In general, $V_{\rm eff}(\ell)$ breaks the N-fold rotational symmetry of the wire, and in addition it can also vary along the chains, i. e., $V_{\rm eff}=V_{\rm eff}(i,\ell)$, but here we do not consider this aspect.

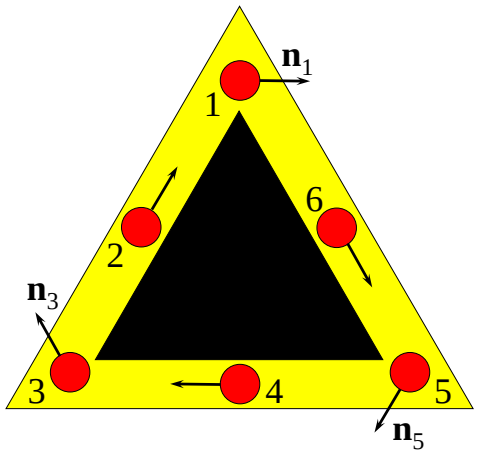

FIG. A1. Schematic representation of the toy model construction for a triangular wire. The shell (yellow/light gray) is coarse-grained so that the vertices and the sides are represented by one-dimensional chains (red/dark gray circles). The arrows indicate the direction of the effective magnetic field n_ℓ associated with the (longitudinal) Rashba spin-orbit coupling.

The term proportional to Γ accounts for the property that the "side states" have higher energies than the "corner states" as shown in Fig. 2. The next term models a Rashba-type SOI, with longitudinal and transverse components proportional to α and α', respectively, generated by an effective electric field in the shell, Fig. 3. The corresponding direction of the effective magnetic field, n_ℓ, for electrons moving along a triangular wire, is shown in Fig. A1. The last two terms in Eq. (A.1) describe the Zeeman splitting $E_Z=g_{\rm eff}\mu_B B$ generated by an external magnetic field applied along the chains, and the proximity-induced pairing. Note that pairing potential Δ_ℓ can be chain-dependent, which reflects the generic situation when the surface of the wire is not uniformly covered by a superconducting layer. Here we shall consider a constant pairing potential, $\Delta=0.3$ meV. The other model parameters used in the numerical calculations presented below have the following values: $t=5.64$ meV, $t'=1.41$ meV, $\alpha=2.0$ meV, $\alpha'=0.5$ meV. In these examples only the corner chains are considered, i. e. with odd ℓ, corresponding to the previous calculations where the chemical potential was always inside the gap Γ.

The first question that we address using the simplified tight-binding model given by Eq. (A.1) concerns the structure of the phase diagram of the proximitized wire. For this purpose we consider a translation-invariant system (i. e., an infinite wire) and, for concreteness, we focus

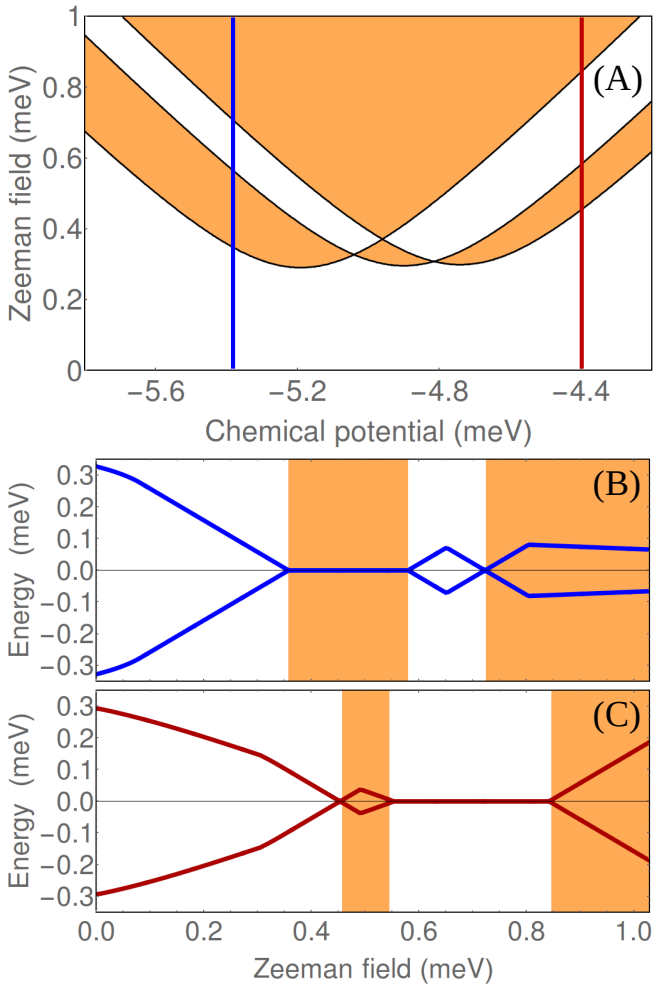

FIG. A2. (A) Topological phase diagram for a symmetric triangular wire, $V_{\rm eff} = 0$. The white areas are topologically trivial, while the orange (gray) regions correspond to $\mathcal{M} = -1$. (B) Dependence of the minimum quasiparticle gap on the Zeeman field for $\mu = -5.4$ meV [blue cut in panel (A)]. (C) Dependence of the minimum quasiparticle gap on the Zeeman field for $\mu = -4.4$ meV [dark red cut in panel (A)]. The white/orange regions correspond to the phases shown in panel (A). Note the vanishing of the quasiparticle gap in certain parameter regions.

on the triangular case, i. e. on the case $N = 3$. To distinguish between the topologically trivial and nontrivial phases, we calculate the $\mathbb{Z}_2$ topological index $\mathcal{M}$ (the so-called *Majorana number*) defined as[1]

$$\mathcal{M} = \text{sign}\left[\text{Pf}\, B(0)\right] \text{sign}\left[\text{Pf}\, B(\pi)\right], \qquad \text{(A.2)}$$

where Pf[...] designate the Pfaffian and $B(k)$ is a momentum-dependent antisymmetric matrix (see below). The trivial phase is characterized by $\mathcal{M} = +1$, while $\mathcal{M} = -1$ signals a topological superconducting phase. The antisymmetric matrix B represents the Fourier transform of the Hamiltonian (A.1) in the Majorana basis and can be constructed[14,50] by virtue of the particle-hole symmetry of the BdG Hamiltonian,

$$\mathcal{T}\mathcal{H}(k)\mathcal{T}^{-1} = \mathcal{H}(-k), \qquad \text{(A.3)}$$

where $H(k)$ is the Fourier transform of the (single particle) Hamiltonian corresponding to Eq. (A.1) and $\mathcal{T} = U_t K$ is the antiunitary time-reversal operator, with U_t being a unitary operator and K the complex conjugation. One can easily verify that $B(k) = \mathcal{H}(k)U_t$ is an antisymmetric matrix when calculated at the time-reversal invariant points $k = 0$ and $k = \pi$. Furthermore, for physically-relevant model parameters (i. e., Zeeman splittings not exceeding a few meVs and chemical potentials near the bottom of the spectrum) we have $\text{sign}\left[\text{Pf}\, B(\pi)\right] = +1$ and the topological phase boundary is determined by a sign change of $\text{Pf}\, B(0)$. Note that $\text{Det}\mathcal{H}(0) = \left[\text{Pf}\, B(0)\right]^2$, hence the phase boundary is associated with the vanishing of the quasiparticle gap at $k = 0$.

The phase diagram for a triangular wire with $V_{\rm eff}(\ell) = 0$ (i. e., no symmetry-breaking potential) is shown in panel (A) of Fig. A2. The white regions are characterized by $\mathcal{M} = +1$, i. e., they are topologically trivial, while the orange (gray) areas correspond to $\mathcal{M} = -1$. The three phase boundaries would merge into a single one, like in Fig. 11(a), if $t'/t \to 0$. For a complementary characterization of different phases, we calculate, as before, the minimum quasiparticle energy (for all wave vectors), as shown in Fig. A2(B-C), for two different values of the chemical potential. At $E_Z = 0$ the system is in a trivial superconducting phase characterized by a quasiparticle gap close to Δ. Increasing E_Z reduces the quasiparticle gap, which eventually vanishes at a certain critical field. In panel (C), the gap reopens as we enter a topological superconducting region (orange). By contrast, in panel (B) the spectrum remains gapless throughout the first region characterized by $\mathcal{M} = -1$, which means that the system is a gapless superconductor. Note that the vanishing of the gap happens at $k \neq 0$, except for the phase boundary crossing points, where the quasiparticle gap vanishes at $k = 0$, as mentioned above. A gapless superconducting phase is also present in panel (C) for Zeeman fields between approximately 0.55 meV and 0.85 meV, where $\mathcal{M} = +1$. Finally, for large-enough values of the Zeeman splitting, i. e. above 0.7 meV in panel (B) and 0.85 meV in panel (C), the system is in a gapped topological phase.

Next, we consider the effect of a symmetry-breaking potential $V_{\rm eff}(\ell) = (0.67, -0.33, -0.33)$ meV for $\ell = 1, 3, 5$. The results are shown in Fig. A3. First, we note that the location of the phase boundaries changes significantly, but the topology of the phase diagram remains the same. Second, upon breaking the three-fold rotation symmetry of the wire the gapless superconducting phases shown in Fig. A2 become gapped. Finally, we note that the low-field topological phase corresponding to $\mu = -4.4$ meV is characterized by a sizable quasiparticle gap [see panel (C)], which suggests that this regime may be particularly suitable for the experimental realization of a topological superconducting state that supports

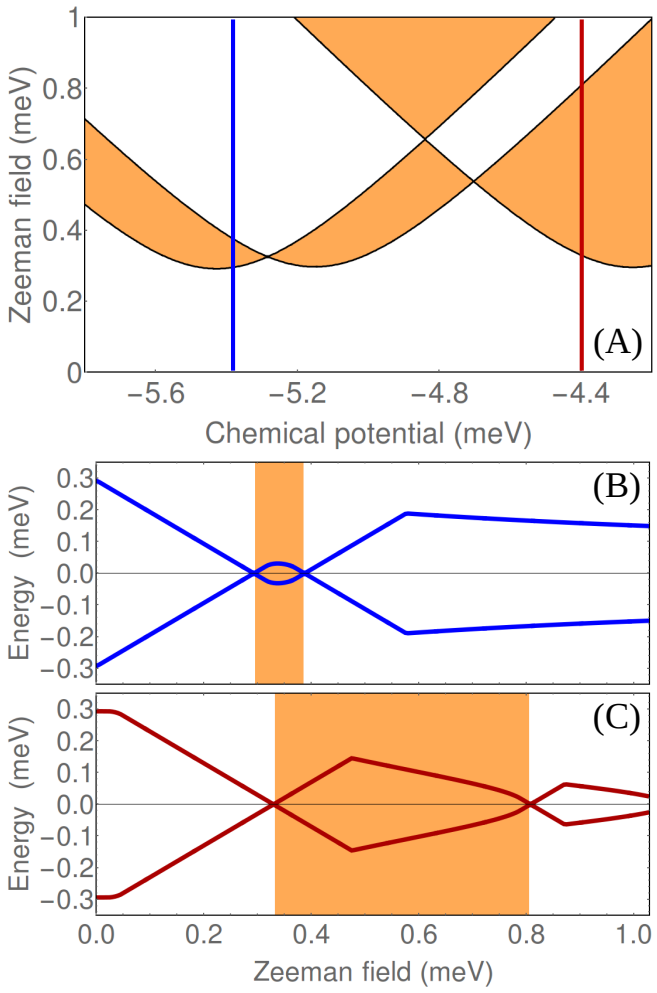

FIG. A3. (A) Topological phase diagram as function of the chemical potential and applied Zeeman field for a slightly asymmetric triangular wire, with $V_{\text{eff}} = (0.67, -0.33, -0.33)$ meV at corners. The white and orange (gray) phases are topologically trivial and nontrivial, respectively. (B) Dependence of the minimum quasiparticle gap on the Zeeman field for $\mu = -5.4$ meV [blue cut in panel (A)]. (C) Dependence of the minimum quasiparticle gap on the Zeeman field for $\mu = -4.4$ meV [dark red cut in panel (A)]. Note that all superconducting phases are gapped.

robust zero-energy Majorana modes.

[1] A. Y. Kitaev, Physics-Uspekhi **44**, 131 (2001).
[2] A. Y. Kitaev, Ann. Phys. **303**, 2 (2003).
[3] F. Wilczek, Nature Phys. **5**, 614 (2009).
[4] C. Nayak, S. H. Simon, A. Stern, M. Freedman, and S. Das Sarma, Rev. Mod. Phys. **80**, 1083 (2008).
[5] S. Das Sarma, M. Freedman, and C. Nayak, Npj Quantum Information **1**, 15001 (2015).
[6] T. D. Stanescu, *Introduction to topological quantum matter and quantum computation* (CRC Press, Taylor & Francis Group, 2017).
[7] L. Fu and C. L. Kane, Phys. Rev. Lett. **100**, 096407 (2008).
[8] J. D. Sau, R. M. Lutchyn, S. Tewari, and S. Das Sarma, Phys. Rev. Lett. **104**, 040502 (2010).
[9] S. Nadj-Perge, I. K. Drozdov, J. Li, H. Chen, S. Jeon, J. Seo, A. H. MacDonald, B. A. Bernevig, and A. Yazdani, Science **346**, 602 (2014).
[10] J. Alicea, Rep. Prog. Phys. **75**, 076501 (2012).
[11] T. D. Stanescu and S. Tewari, J. Phys.: Condens. Matter **25**, 233201 (2013).
[12] C. W. J. Beenakker, Annual Review of Cond. Matt. Phys. **4**, 113 (2013).
[13] M. Franz, Nature Nanotechnology **8**, 149 (2013).
[14] R. M. Lutchyn, J. D. Sau, and S. Das Sarma, Phys. Rev. Lett. **105**, 077001 (2010).

[15] Y. Oreg, G. Refael, and F. von Oppen, Phys. Rev. Lett. **105**, 177002 (2010).

[16] V. Mourik, K. Zuo, S. Frolov, S. Plissard, E. Bakkers, and L. Kouwenhoven, Science **336**, 1003 (2012).

[17] M. Deng, C. Yu, G. Huang, M. Larsson, P. Caroff, and H. Xu, Nano Lett. **12**, 6414 (2012).

[18] A. Das, Y. Ronen, Y. Most, Y. Oreg, M. Heiblum, and H. Shtrikman, Nature Phys. **8**, 887 (2012).

[19] H. Churchill, V. Fatemi, K. Grove-Rasmussen, M. Deng, P. Caroff, H. Xu, and C. Marcus, Phys. Rev. B **87**, 241401 (2013).

[20] A. D. K. Finck, D. J. Van Harlingen, P. K. Mohseni, K. Jung, and X. Li, Phys. Rev. Lett. **110**, 126406 (2013).

[21] W. Chang, S. M. Albrecht, T. S. Jespersen, F. Kuemmeth, P. Krogstrup, J. Nygård, and C. M. Marcus, Nat Nano **10**, 232 (2015).

[22] P. Krogstrup, N. L. B. Ziino, W. Chang, S. M. Albrecht, M. H. Madsen, E. Johnson, J. Nygård, C. M. Marcus, and T. S. Jespersen, Nature Materials **14**, 400 (2015).

[23] S. M. Albrecht, A. P. Higginbotham, M. Madsen, F. Kuemmeth, T. S. Jespersen, J. Nygård, P. Krogstrup, and C. M. Marcus, Nature **531**, 206 (2016).

[24] M. T. Deng, S. Vaitiekenas, E. B. Hansen, J. Danon, M. Leijnse, K. Flensberg, J. Nygård, P. Krogstrup, and C. M. Marcus, Science **354**, 1557 (2016).

[25] H. Zhang, O. Gül, S. Conesa-Boj, K. Zuo, V. Mourik, F. K. de Vries, J. van Veen, D. J. van Woerkom, M. P. Nowak, M. Wimmer, D. Car, S. Plissard, E. P. A. M. Bakkers, M. Quintero-Pérez, S. Goswami, K. Watanabe, T. Taniguchi, and L. P. Kouwenhoven, arXiv:1603.04069 (2016).

[26] J. Chen, P. Yu, J. Stenger, M. Hocevar, D. Car, S. R. Plissard, E. P. Bakkers, T. D. Stanescu, and S. M. Frolov, e-print arXiv:1610.04555 (2016).

[27] T. D. Stanescu, R. M. Lutchyn, and S. Das Sarma, Phys. Rev. B **84**, 144522 (2011).

[28] B. Nijholt and A. R. Akhmerov, Phys. Rev. B **93**, 235434 (2016).

[29] T. Ihn, *Semiconductor nanostructures* (Oxford, 2010).

[30] F. Maier, J. Klinovaja, and D. Loss, Phys. Rev. B **90**, 195421 (2014).

[31] A. Bertoni, M. Royo, F. Mahawish, and G. Goldoni, Phys. Rev. B **84**, 205323 (2011).

[32] H. Wu, D. W. L. Sprung, and J. Martorell, J. Appl. Phys. **72**, 151 (1992).

[33] J. T. Londergan, J. P. Carini, and D. P. Murdock, *Binding and Scattering in Two-Dimensional Systems. Applications to Quantum Wires, Waveguides and Photonic Crystals* (Springer, 1999).

[34] M. Hu, X. Zhang, K. P. Giapis, and D. Poulikakos, Phys. Rev. B **84**, 085442 (2011).

[35] B. M. Wong, F. Lonard, Q. Li, and G. T. Wang, Nano Letters **11**, 3074 (2011).

[36] C. Blömers, T. Rieger, P. Zellekens, F. Haas, M. I. Lepsa, H. Hardtdegen, Ö. Gül, N. Demarina, D. Grützmacher, H. Lüth, and T. Schäpers, Nanotechnology **24**, 035203 (2013).

[37] F. Qian, M. Brewster, S. K. Lim, Y. Ling, C. Greene, O. Laboutin, J. W. Johnson, S. Gradečak, Y. Cao, and Y. Li, Nano Letters **12**, 3344 (2012).

[38] M. Heurlin, T. Stankevič, S. Mickevičius, S. Yngman, D. Lindgren, A. Mikkelsen, R. Feidenhansl, M. T. Borgström, and L. Samuelson, Nano Letters **15**, 2462 (2015).

[39] X. Yuan, P. Caroff, F. Wang, Y. Guo, Y. Wang, H. E. Jackson, L. M. Smith, H. H. Tan, and C. Jagadish, Advanced Functional Materials **25**, 5300 (2015).

[40] A. Sitek, L. Serra, V. Gudmundsson, and A. Manolescu, Phys. Rev. B **91**, 235429 (2015).

[41] K. Pöyhönen, A. Weststrom, J. Röntynen, and T. Ojanen, Phys. Rev. B **89**, 115109 (2014).

[42] R. Wakatsuki, M. Ezawa, and N. Nagaosa, Phys. Rev. B **89**, 174514 (2014).

[43] N. Sedlmayr, J. M. Aguiar-Hualde, and C. Bena, Phys. Rev. B **93**, 155425 (2016).

[44] A. Sitek, G. Thorgilsson, V. Gudmundsson, and A. Manolescu, Nanotechnology **27**, 225202 (2016).

[45] R. Winkler, Physica E: Low-dimensional Systems and Nanostructures **22**, 450 (2004).

[46] A. Bringer and T. Schäpers, Phys. Rev. B **83**, 115305 (2011).

[47] A. Manolescu, T. O. Rosdahl, S. I. Erlingsson, L. Serra, and V. Gudmundsson, The European Physical Journal B **86**, 445 (2013).

[48] J. S. Lim, R. Lopez, and S. L., Europhys. Lett. **103**, 37004 (2013).

[49] L. Serra, Phys. Rev. B **87**, 075440 (2013).

[50] P. Ghosh, J. D. Sau, S. Tewari, and S. Das Sarma, Phys. Rev. B **82**, 184525 (2010).